*Article*

# Hot-Pressing of Ti-Al-N Multiphase Composite: Microstructure and Properties

**Ryszard Sitek [1,*], Kamil Bochenek [2,3], Piotr Maj [4], Michał Marczak [5], Krzysztof Żaba [6], Mateusz Kopec [3], Grzegorz Piotr Kaczmarczyk [7] and Janusz Kamiński [1]**

[1]   Faculty of Materials Science and Engineering, Warsaw University of Technology, Wołoska 141, 02-507 Warsaw, Poland; janusz.kaminski@pw.edu.pl

[2]   Faculty of Power and Aeronautical Engineering, Warsaw University of Technology, 21/25 Nowowiejska Street, 00-665 Warsaw, Poland; kamil.bochenek@pw.edu.pl or kboch@ippt.pan.pl

[3]   Institute of Fundamental Technological Research, Polish Academy of Sciences, Pawińskiego 5B Str, 02-106 Warsaw, Poland; mkopec@ippt.pan.pl

[4]   Faculty of Mathematical & Nature Sciences, Cardinal Stefan Wyszynski University, Sch Exact Sci, Warsaw, Poland, Kazimierza Wóycickiego 1/3. 21, 01-938 Warsaw, Poland; piotr.maj@uksw.edu.pl or piotr.maj@pw.edu.pl

[5]   Faculty of Mechanical and Industrial Engineering, Warsaw University of Technology, Narbutta 85, 02-524 Warsaw, Poland; michal.marczak@pw.edu.pl

[6]   Department of Metal Working and Physical Metallurgy of Non-Ferrous Metals, Faculty of Non-Ferrous Metals, AGH University of Krakow, Al. Adama Mickiewicza 30, 30-059 Cracow, Poland; krzyzaba@agh.edu.pl

[7]   Department of Geomechanics, Civil Engineering and Geotechnics, AGH University of Krakow, Al. Adama Mickiewicza 30, 30-059 Cracow, Poland; grzegorz.kaczmarczyk@agh.edu.pl

*   Correspondence: ryszard.sitek@pw.edu.pl

**Abstract:** This study focuses on the development and characterization of a bulk Ti-Al-N multiphase composite enriched with BN addition and sintered through hot pressing. The research aimed to create a material with optimized mechanical and corrosion-resistant properties suitable for demanding industrial applications. The composite was synthesized using a powder metallurgy approach with a mixture of AlN, TiN, and BN powders, processed under a high temperature and pressure. Comprehensive analyses, including microstructural evaluation, hardness testing, X-ray tomography, and electrochemical corrosion assessments, were conducted. The results confirmed the formation of a multiphase microstructure consisting of TiN, $Ti_2AlN$ and $Ti_3AlN$ phases. The microstructure was uniform with minimal porosity, achieving a hardness within the range of 500–540 HV2. Electrochemical tests revealed the formation of a passive oxide layer that provided moderate corrosion resistance in chloride-rich environment. However, localized pitting corrosion was observed under extreme conditions. The study highlights the potential of a BN admixture to enhance mechanical and corrosion-resistant properties and suggests directions for further optimization in sintering processes and material formulations.

**Keywords:** AlN-TiN(BN) composite; hot-pressing; μCT; corrosion resistance; SEM

## 1. Introduction

The advancement of industry heavily relies on the availability of materials with exceptional functional properties, such as resistance to abrasive wear, corrosion under both low- and high-temperature conditions, and erosion, and high hardness values. The design of new materials or the enhancement of existing ones is a critical driver of technological

progress. In the tool industry, particular emphasis is placed on coatings that exhibit high hardness and resistance to abrasive wear, erosion, and corrosion. Widely used coatings include TiN, TiAlN, TiCN, and diffusion layers of titanium nitride, particularly for cutting tools exposed to extreme mechanical and chemical stresses [1–5]. These coatings and diffusion layers are produced using various deposition technologies, including Chemical Vapor Deposition (CVD) and Physical Vapor Deposition (PVD). These methods enable the creation of coatings with high hardness and excellent wear resistance, making them especially suitable for machining applications [6–10]. However, despite their numerous advantages, these coatings face limitations, particularly in resisting corrosion caused by moisture, seawater salts, and other aggressive chemicals [11].

To overcome these challenges, $Ti_{1-x}Al_xN$ coatings have gained significant attention due to their exceptional resistance to high-temperature oxidation and corrosion and their low thermal conductivity [12–16]. These properties make TiAlN coatings increasingly attractive for cutting tools, especially in wood machining applications. Additionally, the corrosion resistance of TiAlN coatings in neutral and alkaline environments is a critical aspect of their performance. However, structural defects, such as microcracks and pores, remain a challenge as they can act as initiation sites for corrosion [17,18].

The spontaneous formation of oxides on titanium and aluminum alloys imparts excellent corrosion resistance through a nanometric passive layer. However, in highly chlorinated environments, this passive layer becomes susceptible to pitting corrosion. Furthermore, the amphoteric nature of aluminum contributes to the degradation of the oxide layer in low-pH solutions containing aggressive acids such as hydrochloric acid (HCl), sulfuric acid ($H_2SO_4$), or hydrofluoric acid (HF), intensifying corrosion processes. The durability of Ti-Al-N coatings in such environments depends on the aluminum content in the alloy, which influences the quality and stability of the oxide layers [19–21].

Given these considerations, developing advanced technologies to further enhance the protective properties of TiAlN-based coatings is imperative. A promising approach involves utilizing powder metallurgy techniques to produce multiphase composites with improved corrosion resistance and enhanced mechanical properties. Processes such as hot pressing (HP) enable the fabrication of cutting inserts from materials resistant to abrasive wear, corrosion, and erosion. The HP process offers significant advantages, including high repeatability, minimal material waste (near-net-shape processing), and suitability for complex geometries, making it an ideal choice for manufacturing multi-cutting inserts. These advantages are evident in both research and industrial applications to produce cutting tools, where carbides or oxides are sintered to achieve substantial improvements in wear resistance [22,23].

The current study represents one of the first efforts to develop a bulk composite based on TiN, $Ti_2AlN$ and $Ti_3AlN$ enriched with BN—(AlN-TiN(BN)), and to analyze its microstructure, porosity, corrosion resistance, and hardness. The findings confirmed the expected properties, offering valuable insights into the composite's hardness and structural integrity under high-pressure sintering conditions.

## 2. Materials and Methods

### 2.1. Material

In this study, hot-pressed sintered samples were prepared using pre-mixed powder blends. The powder compositions were designated according to the manufacturer's specifications. Prior to consolidation, the powders were analyzed using a scanning electron microscope Zeiss Crossbeam Z350 (Carl Zeiss AG, Oberkochen, Germany) equipped with an X-ray microanalysis system to evaluate their morphology and elemental distribution. The commercial powders used in this research included aluminum nitride (AlN) from H.C. Starck GmbH (Goslar, Germany), titanium nitride (TiN) from KAMB Import-Export (Warsaw, Poland), and boron nitride (ABCR GmbH—Karlsruhe, Germany). The TiN and

AlN powders were mixed in a 2:1 ratio, with the addition of 0.5 wt.% BN, using a planetary ball mill (Fritsch Pulverisette 5, FRITSCH, Idar-Oberstein, Germany). A 250 mL tungsten carbide milling chamber and 10 mm WC grinding balls were employed. The milling process was carried out with a ball-to-powder ratio of 10:1, a rotational speed of 200 rpm, and alternating cycles of 10 min of milling followed by 20 min of cooling. The process concluded after 4 h of milling. Particle size analysis of the processed powders was performed using a Malvern Mastersizer 3000 particle size analyzer (Malvern Instruments Ltd., Malvern, UK). The initial AlN particles (average size 1.65 μm) and TiN particles (average size 14.2 μm) underwent planetary mixing, resulting in a tri-modal particle distribution with an average particle size of 2 μm (Figure 1). A small addition of BN did not significantly affect the particle size distribution. The analysis conducted via Scanning Electron Microscopy (SEM) (Figure 2) confirmed that the particle sizes of the examined powders are highly diverse. The smallest particle diameter was observed for aluminum nitride (Figure 2a). SEM observations of the powder particles also revealed their morphology. Particle analysis (Figure 2b–d) showed that the particles have an angular, sharp-edged, and plate-like structure. The HP sintering process demonstrates minimal dependence on the morphology of the initial powders. Even with a low flowability, a sintered bulk material density exceeding 99% was achieved.
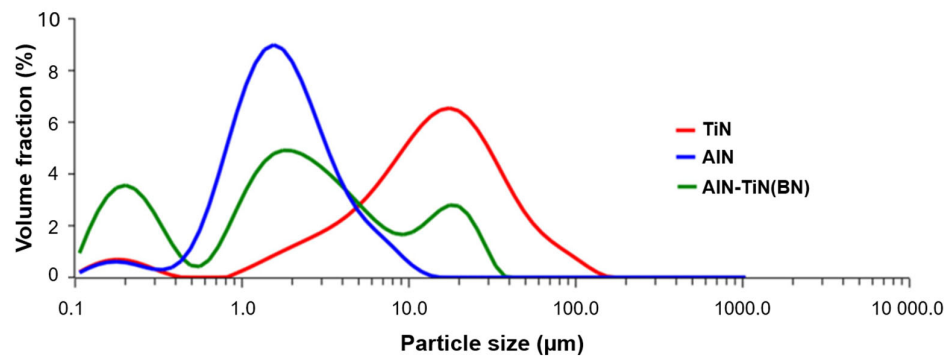


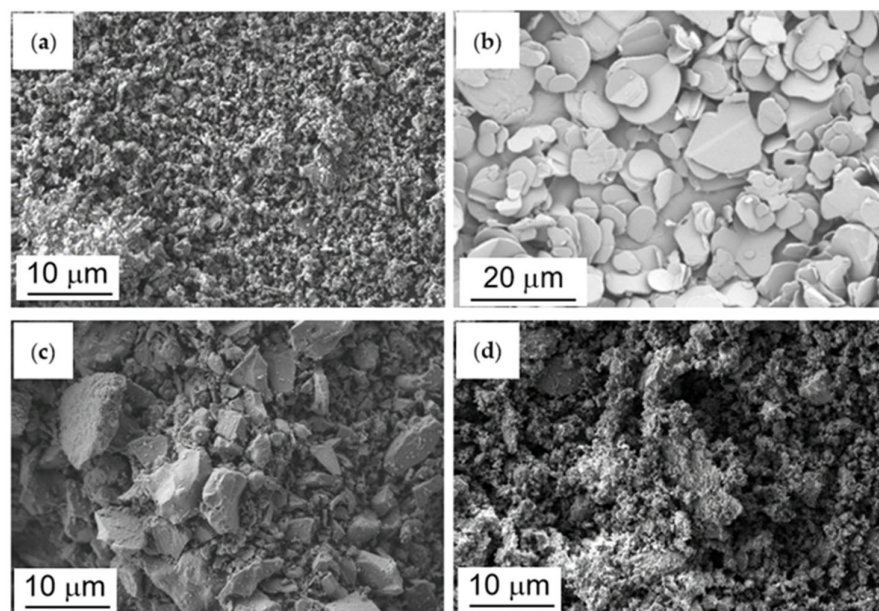**Figure 1.** Particle size distribution of raw TiN and AlN powders along with AlN-TiN(BN) mixture.



**Figure 2.** Powder morphology: (**a**) AlN, (**b**) BN, (**c**) TiN (**c**), and mix of powders (**d**).

## 2.2. Sintering Process

The TiN, AlN and BN powder mixtures were sintered in a hot press (HP, Thermal Technology LLC, Minden, NV, USA) in a vacuum atmosphere. After an optimization process starting at 1100 °C, the final properties were as follows: temperature of 1300 °C, pressure of 30 MPa, and holding time of 60 min along with a heating rate of 10 °C/min. The sample dimensions after removal from the furnace were 14 mm in diameter and about 10 mm in height. Figure 3 shows the sintering process: Pressure is applied from RT until cooling to 500 °C, and then the pressure is released. The heating and cooling rates are the same from RT to 500 °C; then, free cooling occurs.
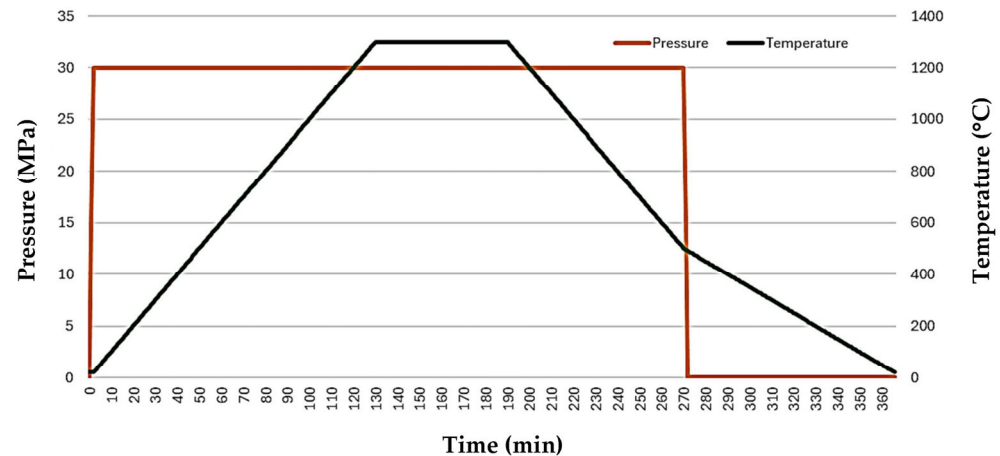


**Figure 3.** Hot pressing—progress of the pressure and temperature during process.

## 2.3. µCT Data Acquisition and Analysis

Industrial tomographic imaging devices (such as XCT, µCT, and X-ray CT) function based on the principles of X-ray spectroscopy, as extensively detailed in various publications [21,24]. Despite being developed over two decades ago, the technology's core mechanisms remain essential and widely utilized. The imaging process involves analyzing a target object placed in a specialized chamber positioned between the radiation source (commonly referred to as the tube) and the detector. The device operates by precisely adjusting the object's position relative to the source and detector, setting the appropriate voltage and current intensity to control the radiation output, and configuring detector parameters. Fine-tuning these settings ensures the collection of high-quality data suitable for quality analysis and enables detection of material defects like pores in the whole volume of the material. For this study, data were collected using a microfocus X-ray tube operating at 100 kV and 95 µA, yielding voxel dimensions of 9.53 µm$^3$.

The next phase entails reconstructing the 3D structure of the scanned object. As the sample completes a full rotation, the system generates numerous high-resolution grayscale images, such as those produced by the GE Phoenix v|tomex|m system (General Electric Company, Hürth, Germany), which features a 14-bit grayscale depth. Advanced algorithms are employed during reconstruction, incorporating features such as beam hardening correction, automated geometry calibration, and geometry refinement [25,26]. The resulting reconstructed models enable detailed analyses, including 2D and 3D cross-sectional imaging and volumetric studies. In this study, reconstruction was performed using an established algorithm that applied the BHC+ filter (factor 6.4), automatic AGC, and optimized reconstruction parameters. The volumetric analysis commenced with identifying the material's isosurface, distinguished by its higher density. Porosity was evaluated using the VGDefX procedure in VGStudio MAX 3.5.1. Total sample porosity was

quantified, with significant defects defined as regions exceeding eight voxels. After further filtering, only large-scale defects (0.02 mm$^3$ or larger) were included in the final analysis.

### 2.4. Corrosion Resistance

The corrosion resistance of the multiphase AlN-TiN(BN) sintered composite was evaluated using electrochemical impedance spectroscopy (EIS) and linear sweep voltammetry (LSV). The tests were conducted with an AutoLab PGSTAT 100 potentiostat (Eco Chemie B.V., Utrecht, The Netherlands) in a non-deaerated aqueous solution of 1 M NaCl (pH 6.7) at room temperature. Prior to the electrochemical measurements, the samples were immersed in the corrosive solution at the open circuit potential (OCP) for 3600 s to allow for the stabilization of the corrosion potential. Impedance measurements were performed in a three-electrode setup comprising the test electrode, a reference electrode (saturated calomel electrode, SCE), and an auxiliary electrode (platinum). The frequency range spanned from $10^5$ to $10^{-3}$ Hz, using an AC signal with an amplitude of 10 mV. The corrosion cell was placed inside a Faraday cage to prevent external interference. Electrochemical impedance spectroscopy (EIS) data were recorded in potentiostatic mode at the open circuit potential ($E_{OCP}$).

The obtained impedance spectra were presented as Bode plots and analyzed using Boukamp's EQUIVCRT software (4.9.007). A two-time-constant equivalent circuit model R(Q[R(RQ)]) was employed for spectral interpretation, a configuration commonly applied for substrates prone to localized corrosion.

Potentiodynamic polarization tests were conducted in the same three-electrode configuration, up to a potential of 2500 mV. The material was polarized at a potential sweep rate of 0.2 mV/s.

## 3. Results and Discussion

### 3.1. Microstructure, Chemical, and Phase Composition Analysis

Figure 4 shows an SEM (BSE—backscattered electrons) image of the composite's microstructure, produced via the hot pressing method using a powder mixture of AlN:TiN in a 1:1 weight ratio, with the addition of 0.5 wt.% boron nitride (AlN-TiN(BN)). The composite exhibits a complex structure characterized by distinct light and dark regions, indicative of variations in chemical composition. No cracks or pores are visible on the sintered material's analyzed surface. The microarea chemical composition analysis indicates that the dark regions predominantly consist of aluminum and nitrogen, with high peak intensities confirming the presence of aluminum nitride (Figure 5a), which remains stable during sintering. The lighter regions display a higher titanium content and significantly lower levels of aluminum and nitrogen, suggesting the presence of a ternary MAX phase (Figure 5b). Quantitative analysis was not conducted due to potential inaccuracies caused by the presence of boron, which is challenging to measure precisely with EDS, and nitrogen, which overlaps with titanium signals. EDS mapping highlights the composite's intricate structure, including undissolved AlN particles that persist after sintering (Figure 6). Phase composition analysis via XRD identifies the presence of $Ti_2AlN$, $Ti_3AlN$, and TiN phases (Figure 7).
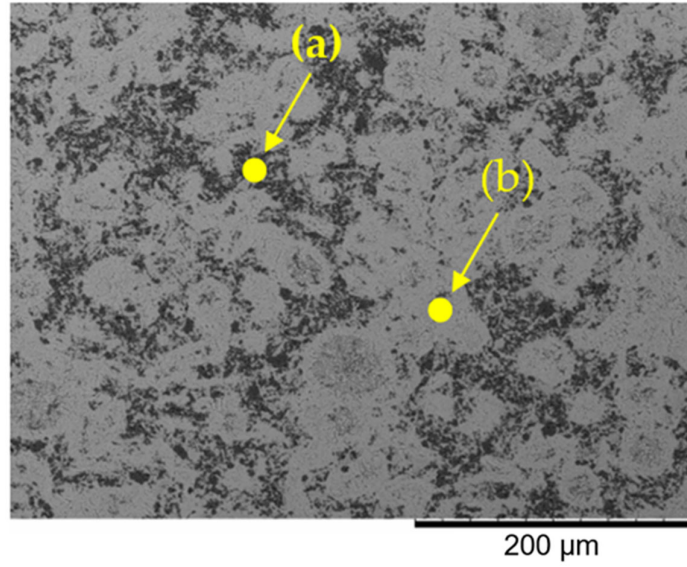
**Figure 4.** SEM BSE micrographs and examined microareas (point a and point b) of the chemical composition (EDS).
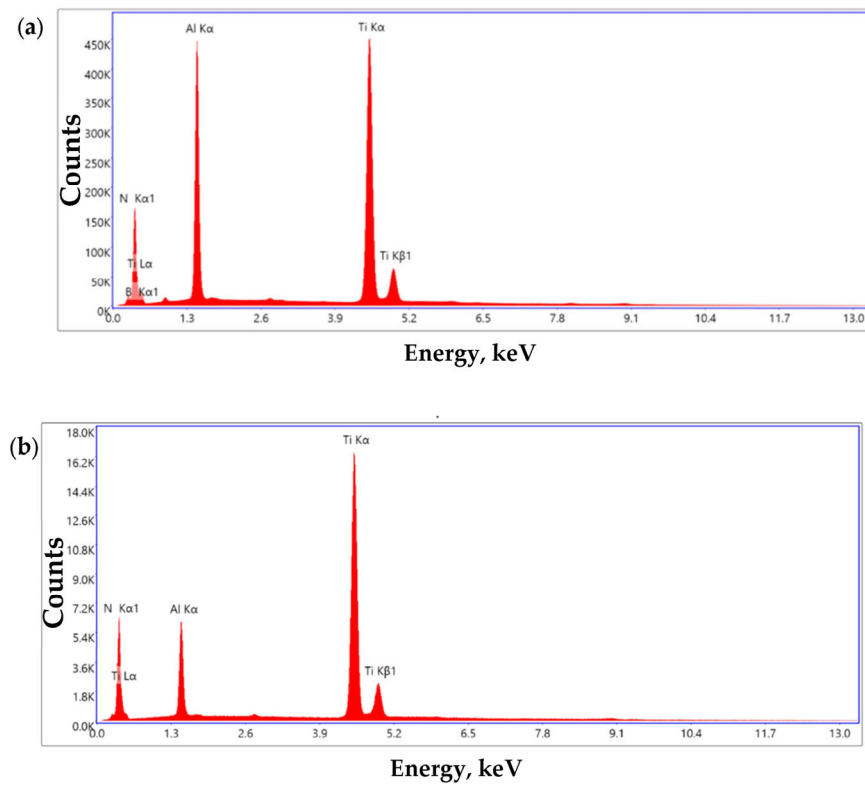




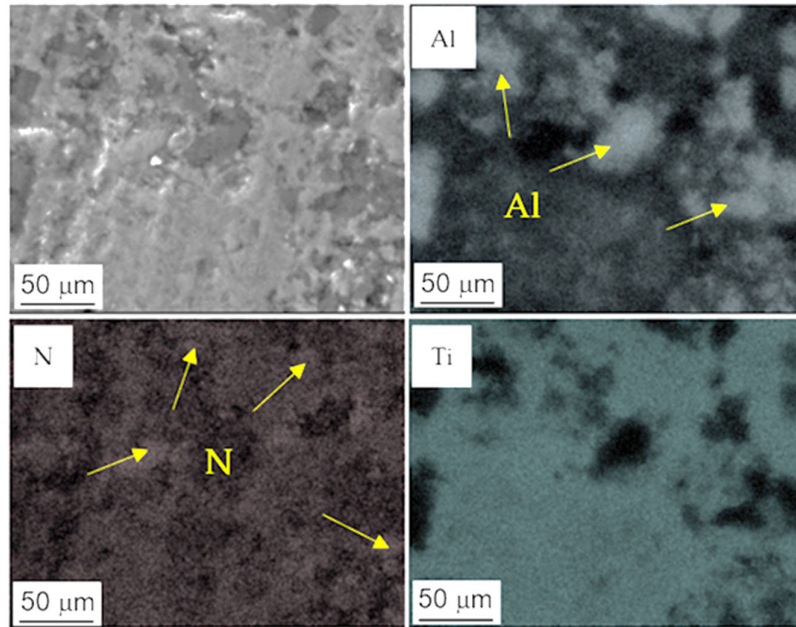**Figure 5.** EDS spectrograms: examined microareas (**a**) and (**b**) from Figure 4.

**Figure 6.** Distribution of elements (Al, Ni, Ti) across the cross-section of the composite after hot processing.
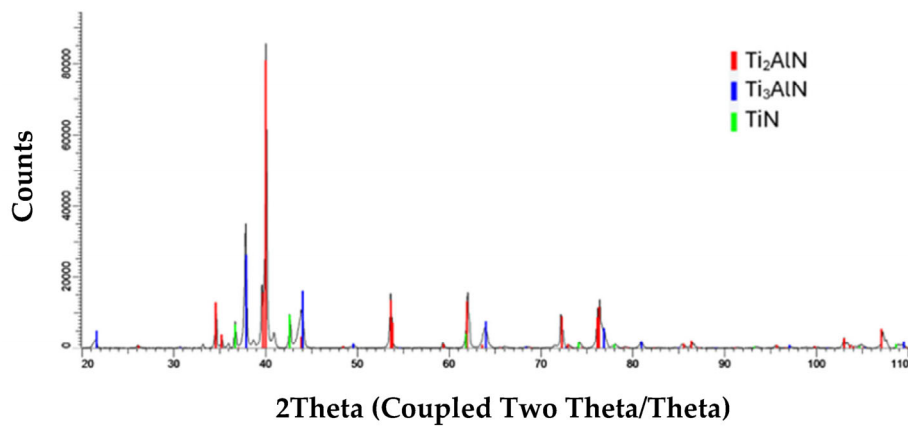


**Figure 7.** X-ray diffraction patterns of AlN-TiN(BN) composite sintered by hot pressing.

### 3.2. CT Analysis

Example cross-sections are presented in Figure 8. Bright colors represent regions of higher density, while darker colors indicate lower density. The structure of the material is heterogeneous, with numerous small, isolated regions of lower density clearly visible. While these observed defects may initially resemble data noise, their distribution strongly suggests the physical presence of such defects. These defects coalesce to form larger regions of lower density, several of which are marked with red arrows in Figure 9.
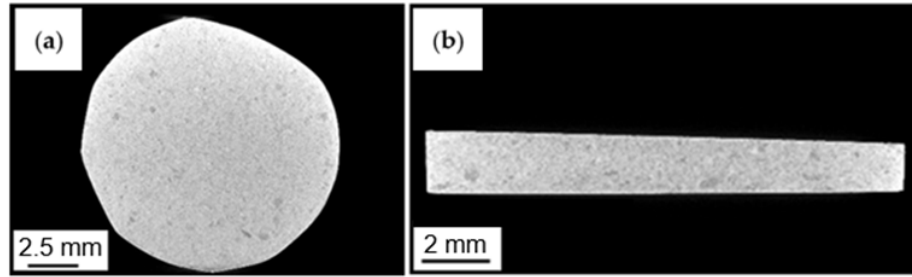
**Figure 8.** Tomographic cross-sections: (**a**) front; (**b**) top view.

A 3D visualization of the data is shown in Figure 9a–c, with each image depicting the same perspective. The analysis identified approximately 530,000 defects, characterized by a low sphericity, accounting for 6.77% of the material's total volume. Individual zones reveal defects merging into larger regions. Filtering for defects larger than 0.02 mm³ yielded 35 distinct volumes. These defects exhibit elongation in the XZ plane, and the 35 largest defects collectively constitute 0.48% of the sample's total volume.
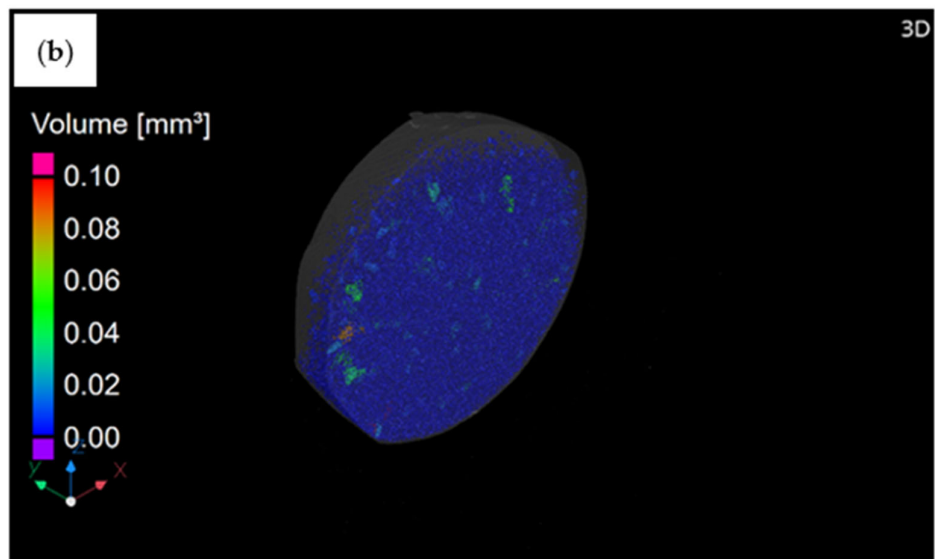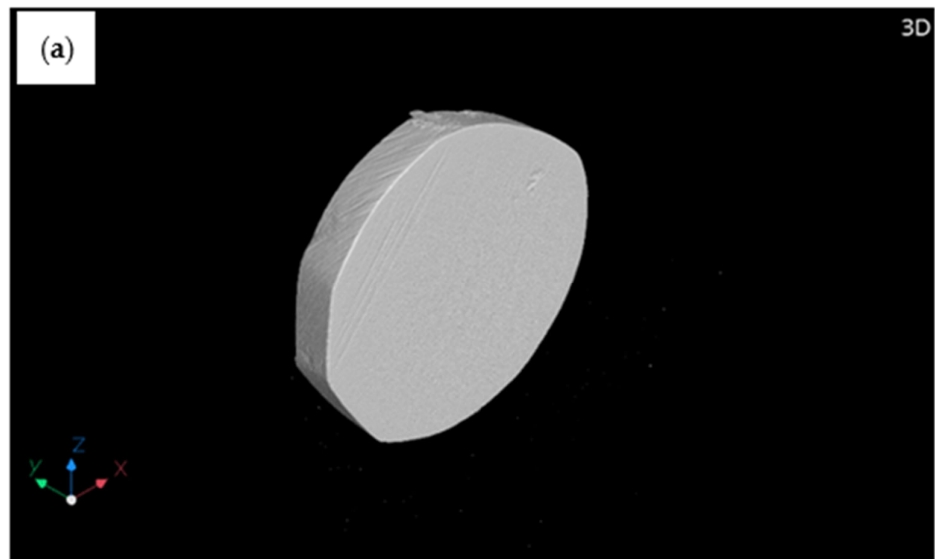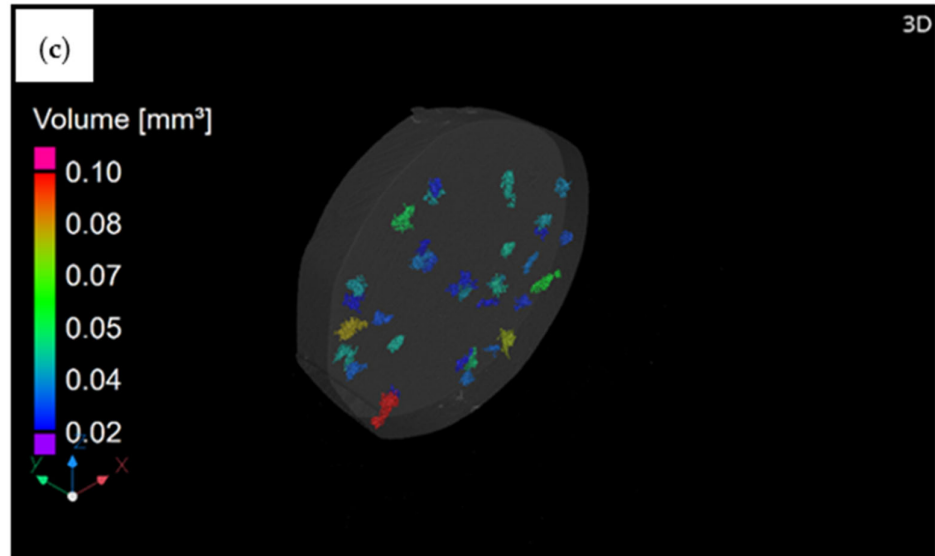
**Figure 9.** Three-dimensional data view: (**a**) sample, (**b**) distribution of all of defects, (**c**) and defects > 0.02 mm$^3$.

### 3.3. Hardness Measurements

Figure 10 illustrates the hardness distribution of the sintered material along the X direction (0 to 25 mm). The results show moderate variations, with hardness values ranging from approximately 500 HV2 to 540 HV2. Despite these fluctuations, the overall hardness profile indicates a relatively homogeneous material structure. The standard deviations, represented by error bars, suggest localized deviations potentially caused by microstructural inconsistencies or variations in processing conditions. However, the absence of significant outliers demonstrates that the material maintains consistent mechanical properties across the measured region, supporting its suitability for applications requiring uniform hardness.
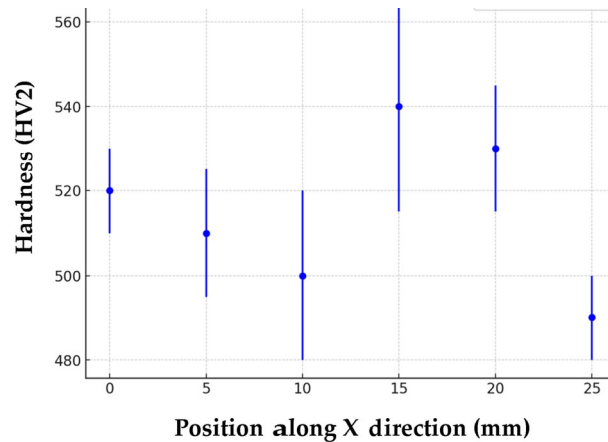


**Figure 10.** Hardness distribution on the sample cross-section.

### 3.4. Corrosion Response Analysis

Electrochemical studies, including electrochemical impedance spectroscopy (EIS) and linear sweep voltammetry (LSV), confirmed the susceptibility of the sintered AlN-TiN(BN) alloy to pitting corrosion. EIS spectra, presented in Figure 11, reveal at least two

overlapping capacitive loops, indicative of distinct electrochemical processes occurring on the examined substrate.
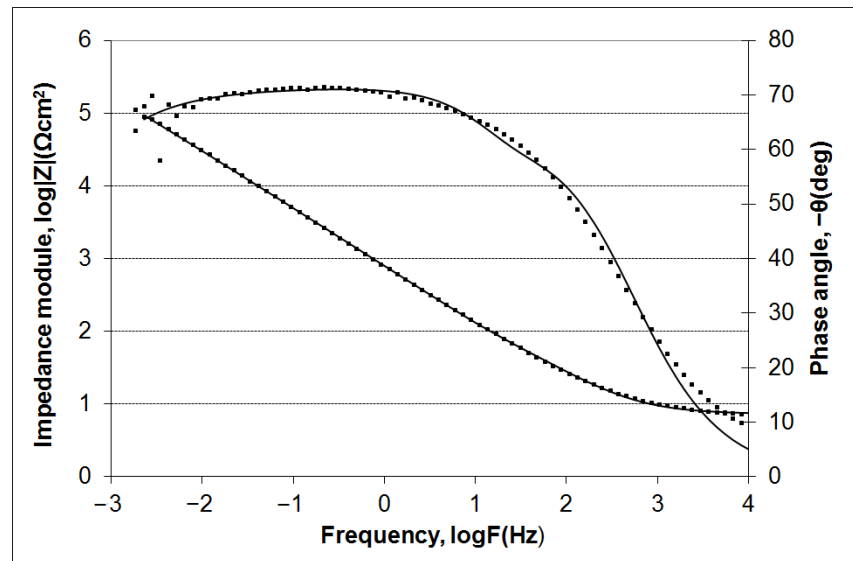


**Figure 11.** Bode plot of the sintered AlN-TiN(BN) composite exposed to 1 M NaCl solution. Solid line—fit; dotted line—experimental data.

The presence of a maximum phase angle over a wide frequency range ($10^{-2}$ Hz to $10^{1}$ Hz) suggests the formation of a passive layer on the alloy surface. However, the relatively low phase angle values ($-\theta = 70°$) indicate reduced capacitive characteristics of the passive film ($\eta = 0.93$). Additionally, the low dielectric resistance of the layer (Table 1) results in a limited passive region which can be observed in potentiodynamic studies (Figure 12), spanning only ~200 mV. The electrochemical parameters of the dielectric layer ($\eta = 0.77$, R = 375 $\Omega$) indicate its active dissolution in a 1 M NaCl solution.

**Table 1.** Characteristic electrochemical parameters of the investigated sintered alloy (EIS measurements).

| | | Environment | Dielectric Layer | Double Layer |
|---|---|---|---|---|
| | R ($\Omega cm^2$) | 7 | $3.75 \times 10^2$ | $9.85 \times 10^5$ |
| $Q_{CPE}$ | $Y_{0\ CPE}$ ($Fcm^{-2}\ s^{n-1}$) | | $2.65 \times 10^{-4}$ | $2.83 \times 10^{-5}$ |
| | n | | 0.77 | 0.93 |

R—resistance; $Q_{CPE}$—capacity of the constant phase element; $Y_{0CPE}$—admittance; n—coefficient of imperfections of the constant phase element (CPE), an empirical constant ranging from 0 to 1. It is worth noting that when n = 1, the CPE behaves as a pure capacitor, while when n = 0, the CPE behaves as a pure resistor.

The potentiodynamic study, the results of which are shown in Figure 12, confirms the material's susceptibility to pitting corrosion. Figure 13 presents the surface topography (SEM image) after potentiodynamic testing in a 1 M NaCl solution, showing numerous deep pits distributed across the surface. Additionally, etched regions of the passive layer are visible between the pits.
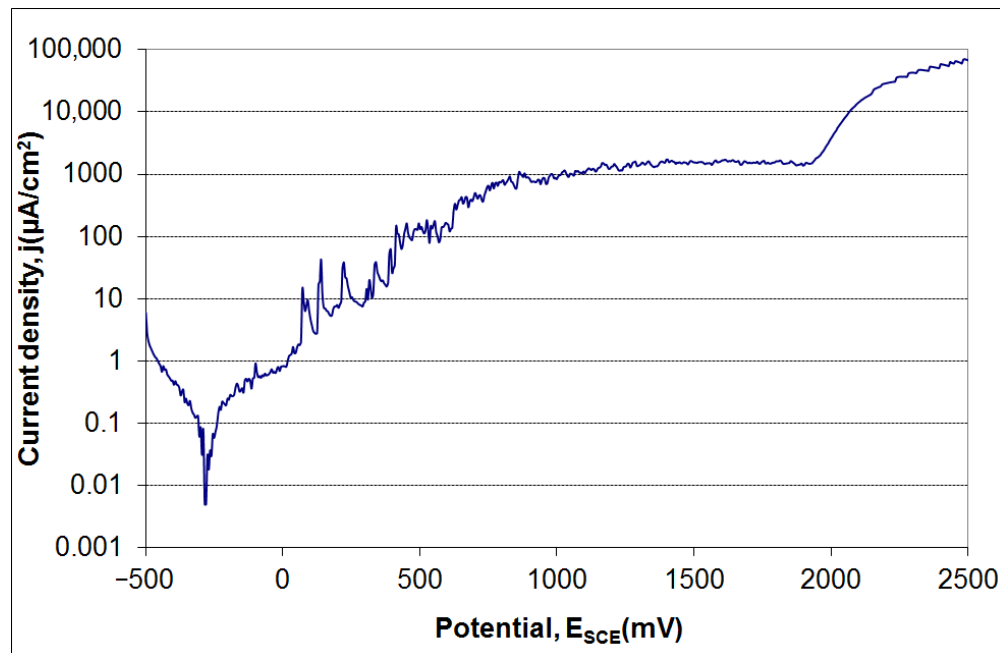
**Figure 12.** Potentiodynamic curves of sintered AlN-TiN(BN) composite exposed to 1 M NaCl at room temperature.

Analysis of the potentiodynamic curve (Figure 12) for the sintered AlN-TiN(BN) composite indicates the presence of a marginally stable passive state, with the passive layer persisting up to approximately 30 mV. Beyond this potential, anodic polarization initiates the formation of metastable pits, which continue up to ~600 mV. The steady increase in current density within this range is attributed to the nitrides (TiN, AlN) in the alloy. These nitrides promote substrate oxidation during anodic polarization, leading to the formation of mixed oxide–nitride phases (e.g., TiNO and AlNO) on the surface. A significant rise in current density beyond 2000 mV corresponds to the onset of pitting corrosion. Electrochemical parameters characterizing the material are summarized in Table 2.

**Table 2.** Electrochemical properties of sintered AlN-TiN(BN) composite (LSV measurements).

| | Corrosion Potential, $E_{corr}$. (mV) | Corrosion Current Density, $I_{corr}$. ($\mu A/cm^2$) |
|---|---|---|
| AlN-TiN(BN) | −285 | 0.078 |

A comparison with published data reveals notable differences in the corrosion resistance of AlN-TiN(BN) composite materials fabricated through various techniques. For instance, Ti-AlN substrates produced via 3D printing methods [27] exhibit no pitting corrosion within the studied potential range (up to 1500 mV vs. SSCE). However, their corrosion resistance is compromised by a dendritic microstructure, multiphasic nature, and prevalent cracking. Sintered materials exhibit a different microstructure (Figure 13) that, in the presence of chloride ions (1 M NaCl), facilitates the initiation of pitting corrosion, as observed in electrochemical testing. Nevertheless, the applied sintering process (temperature: 1300 °C) promotes the formation of a passive layer through the self-passivating behavior of alloy components (Ti, Al), providing improved corrosion resistance compared to 3D-printed materials.
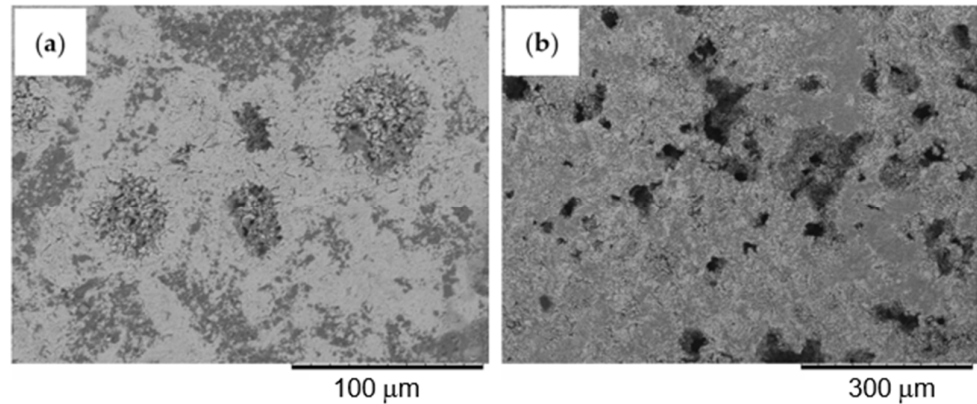
**Figure 13.** Surface topography of the sintered AlN-TiN(BN) alloy before (**a**) and after (**b**) corrosion tests in 1 M NaCl.

The microstructure of the sintered AlN-TiN(BN) composite indicates that, due to the heterogeneity of the initial powder, complete homogeneity was not achieved (Figure 13a). This non-uniformity fosters galvanic corrosion in regions with high electrochemical heterogeneity. Furthermore, due to the high concentration of chloride ions (35.45 g Cl/dm³) in the corrosive solution, pitting corrosion predominantly occurs in areas enriched with oxides/nitrides of substrate components, which are particularly susceptible to halide-induced degradation (Figure 13b).

The corrosion resistance of AlN-TiN(BN) composites was evaluated in a neutral solution (pH 6.7) at room temperature (20 °C). It can be inferred that the corrosion behavior of these materials will vary significantly under extreme pH conditions. This is particularly evident in metals that rely on the formation of a passive layer for corrosion resistance, where changes in pH can lead to alterations in corrosion rates. For example, in amphoteric metals such as aluminum, both decreasing and increasing the pH of the solution may result in the breakdown of the passive layer, thereby increasing the corrosion rate. In titanium alloys, an increase in pH enhances the corrosion resistance of the material by strengthening the passive oxide layer that forms on the surface. Conversely, a high concentration of hydrogen ions at low pH promotes the dissolution of the passive layer and causes the metal to transition to an active state, which accelerates the corrosion rate. For AlN-TiN(BN) composites, the effect of pH on the corrosion rate is influenced by the titanium and aluminum content. In acidic solutions, lowering the pH generally accelerates the corrosion rate. However, in alkaline environments, the corrosion behavior is determined by the relative amounts of titanium and aluminum in the composite. In composites with a higher aluminum content, the corrosion rate tends to increase with higher pH values, while for composites dominated by titanium, an increase in pH leads to improved corrosion resistance.

Temperature is another significant factor influencing the corrosion rate. According to the Arrhenius equation, an increase in temperature accelerates electrochemical reactions, including the rate of corrosion. In aqueous environments, the corrosion rate increases with temperature up to approximately 80 °C. Above this temperature, the corrosion rate decreases gradually due to the reduced solubility of oxygen in water, limiting the availability of dissolved oxygen, which is essential for corrosion processes.

Sintered AlN-TiN(BN) composites generally demonstrate high corrosion resistance, particularly in environments with moderate temperatures and mildly corrosive agents. Their primary protective mechanism involves the formation of a stable oxide layer, conferring resistance to oxidation and wear. Under extreme conditions, such as exposure to strong acids, high chloride concentrations, or elevated temperatures, localized corrosion

or degradation of the oxide layer may occur. Enhanced sintering processes, alloying strategies, and tailored post-treatments can further improve the corrosion resistance of these materials, broadening their application potential in demanding environments. Small admixtures of BN were not detected by the analytical methods used; a broader spectrum of composition needs to be evaluated to directly define the influence of boron nitride on TiN-AlN systems. The presented provide a basis for further research into the introduction of a BN admixture that can improve sintering of the bulk material.

## 4. Conclusions

The main findings of the research were as follows:

- The hot pressing process successfully synthesized a AlN-TiN(BN) composite with a uniform and dense microstructure. The addition of boron nitride significantly influenced the distribution of phases and contributed to the overall integrity of the material.
- The composite exhibited desirable mechanical properties, including a homogeneous hardness distribution (500–540 HV2), suitable for industrial applications requiring durable cutting tools. These properties result from the synergistic interaction of the TiN, $Ti_2AlN$, $Ti_3AlN$, and BN phases within the matrix.
- Electrochemical analysis demonstrated that the composite forms a passive oxide layer in neutral chloride environments, providing a moderate level of protection. However, under high chloride concentrations, localized pitting corrosion was evident, primarily in regions of electrochemical heterogeneity.
- Despite the promising results, improvements are needed to fully integrate the benefits of BN admixture. Future studies should focus on refining sintering parameters and exploring post-treatment processes to enhance corrosion resistance and mechanical durability, particularly in aggressive environments.

**Institutional Review Board Statement:** Not applicable.

**Informed Consent Statement:** Not applicable.

**Data Availability Statement:** Data are contained within the article.

**Conflicts of Interest:** The authors declare no conflicts of interest.

# References

1.  Fan, G.; Zhang, J.; Chen, H.; Xiao, G.; Chen, Z.; Yi, M.; Xu, C.; Fan, L.; Li, G. Analysis of tool wear of TiAlN coated tool, machined surface morphology and chip during titanium alloy milling. *Tribol. Int.* **2024**, *197*, 109751. https://doi.org/10.1016/j.triboint.2024.109751.

2.  Andersen, K.N.; Bienk, E.J.; Schweitz, K.O.; Reitz, H.; Chevalier, J.; Kringhoj, P.; Bottiger, J. Deposition, microstructure and mechanical and tribological properties of magnetron sputtered TiN/TiAlN multilayers. *Surf. Coat. Technol.* **2000**, *123*, 219–226. https://doi.org/10.1016/S0257-8972(99)00473-9.

3.  Smith, I.J.; Gillibrand, D.; Brooks, J.S.; Munz, W.D.; Harvey, S.; Goodwin, R. Dry cutting performance of HSS twist drills coated with improved TiAlN. *Surf. Coat. Technol.* **1997**, *90*, 164–171. https://doi.org/10.1016/S0257-8972(96)03113-1.

4.  Yoon, S.Y.; Kim, J.K.; Kim, K.H. A comparative study on tribological behavior of TiN and TiAlN coatings prepared by arc ion plating technique. *Surf. Coat. Technol.* **2002**, *161*, 237–242. https://doi.org/10.1016/S0257-8972(02)00474-7.

5.  Wang, D.Y.; Chang, C.L.; Wong, K.W.; Li, Y.W.; Ho, W.Y. Improvement of the interfacial integrity of (Ti, Al)N hard coatings deposited on high speed steel cutting tools. *Surf. Coat. Technol.* **1999**, *120–121*, 388–394. https://doi.org/10.1016/S0257-8972(99)00452-1.

6.  Keunecke, M.; Stein, C.; Bewilogua, K.; Koelker, W.; Kassel, D.; van den Berg, H. Modified TiAlN coatings prepared by d.c. pulsed magnetron sputtering. *Surf. Coat. Technol.* **2010**, *205*, 1273–1278. https://doi.org/10.1016/j.surfcoat.2010.09.023.

7.  Matei, A.A.; Pencea, I.; Branzei, M.; Trancă, D.E.; Ţepeş, G.; Sfet, C.E.; Ciovica, E.; Gherghilescu, A.I.; Stanciu, G.A. Corrosion resistance appraisal of TiN, TiCN and TiAlN coatings deposited by CAE-PVD method on WC-Co cutting tools exposed to artificial sea water. *Appl. Surf. Sci.* **2015**, *358*, 572–578. https://doi.org/10.1016/j.apsusc.2015.08.041.

8.  Nnaji, M.O.; Tavakoli, D.A.; Hitchcock, D.A.; Vogel, E.M. Low-temperature formation of $Ti_2AlN$ during post-deposition annealing of reactive multilayer systems. *J. Appl. Phys.* **2024**, *136*, 115302. https://doi.org/10.1063/5.0230405.

9.  He, Q.; Paiva, J.M.; Kohlscheen, J.; Beake, B.D.; Veldhuis, S.C. An integrative approach to coating/carbide substrate design of CVD and PVD coated cutting tools during the machining of austenitic stainless steel. *Ceram. Int.* **2020**, *46*, 5149–5158. https://doi.org/10.1016/j.ceramint.2019.10.259.

10. Liu, L.; Zhou, L.; Tang, W.; Ruan, Q.; Li, X.; Wu, Z.; Qasim, A.M.; Cui, S.; Li, T.; Tian, X.; et al. Study of TiAlN coatings deposited by continuous high power magnetron sputtering (C-HPMS). *Surf. Coat. Technol.* **2020**, *402*, 126315. https://doi.org/10.1016/j.surfcoat.2020.126315.

11. Ananthakumar, R.; Subramanian, B.; Kobayashi, A.; Jayachandran, M. Electrochemical corrosion and materials properties of reactively sputtered TiN/TiAlN multilayer coatings. *Ceram. Int.* **2012**, *38*, 477-485. https://doi.org/10.1016/j.ceramint.2011.07.030.

12. PalDey, S.; Deevi, S.C. Single layer and multilayer wear resistant coatings of (Ti, Al)N: A review. *Mater. Sci. Eng. A* **2003**, *342*, 58–79. https://doi.org/10.1016/S0921-5093(02)00259-9.

13. Chen, L.; Paulitsch, J.; Du, Y.; Mayrhofer, P.H. Thermal stability and oxidation resistance of Ti–Al–N coatings. *Surf. Coat. Technol.* **2012**, *206*, 2954–2960. https://doi.org/10.1016/j.surfcoat.2011.12.028.

14. Hörling, A.; Hultman, L.; Oden, M.; Sjölen, J.; Karlsson, L. Mechanical properties and machining performance of $Ti_{1-x}Al_xN$-coated cutting tools. *Surf. Coat. Technol.* **2005**, *191*, 384–392. https://doi.org/10.1016/j.surfcoat.2004.04.056.

15. Mayrhofer, P.H.; Hörling, A.; Karlsson, L.; Sjölen, J.; Larsson, T.; Mitterer, C.; Hultman, L. Self-organized nanostructures in the Ti–Al–N system. *Appl. Phys. Lett.* **2003**, *83*, 2049–2051. https://doi.org/10.1063/1.1608464.

16. Walczak, M.; Pasierbiewicz, K.; Szala, M. Adhesion and mechanical properties of TiAlN and AlTiN magnetron sputtered coatings deposited on the DMSL titanium alloy substrate. *Acta Phys. Pol. A* **2019**, *136*, 294–298. https://doi.org/10.12693/APhysPolA.136.294.

17. Ibrahim, M.A.M.; Korablov, S.F.; Yoshimura, M. Corrosion of stainless steel coated with TiN, (TiAl)N and CrN in aqueous environments. *Corros. Sci.* **2002**, *44*, 815–828. https://doi.org/10.1016/S0010-938X(01)00102-0.

18. Kayali, Y. The corrosion and wear behavior of TiN and TiAlN coated AISI 316 L stainless steel. *Prot. Met. Phys. Chem. Surf.*, **2014**, *50*, 412–419. https://doi.org/10.1134/S207020511403006X.

19. Tkadletz, M.; Hofer, C.; Wüstefeld, C.; Schalk, N.; Motylenko, M.; Rafaja, D.; Holzschuh, H.; Bürgin, W.; Sartory, B.; Mitterer, C.; et al. Thermal stability of nanolamellar fcc-Ti1-xAlxN grown by chemical vapor deposition. *Acta Mater.* **2019**, *174*, 195–205. https://doi.org/10.1016/j.actamat.2019.05.044.

20. Dobrzański, L.A.; Lukaszkowicz, K.; Zarychta, A.; Cunha, L. Corrosion resistance of multilayer coatings deposited by PVD techniques onto the brass substrate. *J. Mater. Process. Technol.* **2005**, *164–165*, 816–821. https://doi.org/10.1016/j.jmatprotec.2005.02.081.

21. Stock, S.R. X-ray microtomography of materials. *Int. Mater. Rev.* **1999**, *44*, 141–164. https://doi.org/10.1179/095066099101528261.

22. Akhtar, S.S.; Laghari, R.A.; Alotaibi, A.D.; Abubakar, A.A.; Mekid, S.; Al-Athel, K.S. A critical review on functionally graded ceramic materials for cutting tools: Current trends and future prospects. *Rev. Adv. Mater. Sci.* **2023**, *62*, 20230141. https://doi.org/10.1515/rams-2023-0141.

23. Hu, C.; Li, F.; Qu, D.; Wang, Q.; Xie, R. Developments in Hot Pressing and Hot Isostatic Pressing of Ceramic Composites. *Mater. Sci. Eng. A* **2013**, *205*, 164–172. https://doi.org/10.1533/9780857098825.1.164.

24. Kaczmarczyk, G.P.; Cała, M. Possible Application of Computed Tomography for Numerical Simulation of the Damage Mechanism of Cementitious Materials—A Method Review. *Buildings* **2023**, *13*, 587. https://doi.org/10.3390/buildings13030587.

25. Brabant, L.; Pauwels, E.; Dierick, M.; Van Loo, D.; Boone, M.A.; Van Hoorebeke, L. A novel beam hardening correction method requiring no prior knowledge, incorporated in an iterative reconstruction algorithm. *NDT&E Int*. **2012**, *51*, 68–73. https://doi.org/10.1016/j.ndteint.2012.07.002.

26. Nguyen, V.; Sanctorum, J.G.; Van Wassenbergh, S.; Dirckx, J.J.J.; Sijbers, J.; De Beenhouwer, J. Geometry Calibration of a Modular Stereo Cone-Beam X-ray CT System. *J. Imaging* **2021**, *7*, 54. https://doi.org/10.3390/jimaging7030054.

27. Chlewicka, M.; Dobkowska, A.; Sitek, R.; Adamczyk-Cieślak, B.; Mizera, J. Microstructure and corrosion resistance characteristics of Ti–AlN composite produced by selective laser melting. *Mater. Corros*. **2022**, *73*, 451–459. https://doi.org/10.1002/maco.202112703.